

Mean mass transport in an orbitally shaken cylindrical container

Julien Bouvard¹, Wietze Herreman², and Frédéric Moisy¹

¹*Laboratoire FAST, Univ. Paris-Sud, CNRS,
Université Paris-Saclay, 91405 Orsay, France. and*

²*Laboratoire LIMSI, CNRS, Univ. Paris-Sud,
Université Paris-Saclay, 91405 Orsay, France.*

(Dated: May 24, 2022)

A liquid-filled container in orbital shaking motion, i.e. in circular translation with fixed orientation with respect to an inertial frame of reference, generates, in addition to a rotating sloshing wave, a mean flow rotating in the same direction as the wave. Here we investigate experimentally the structure and the scaling of this mean flow in the weakly nonlinear regime, for small forcing amplitude and for forcing frequency far from the resonance, using conventional and stroboscopic particle image velocimetry. In addition to a robust global rotation near the center, the mean flow is composed of a non-trivial pattern of poloidal recirculation vortices of weaker amplitude, mostly active near the contact line. The amplitude of the global rotation near the center is well described by a simple weakly nonlinear scaling with weak influence of viscosity, suggesting that the Stokes drift provides the dominant contribution to this component of the Lagrangian mean flow. On the other hand, the spatial structure of the poloidal vortices show strong variation with viscosity and forcing frequency, suggesting a subtle response of the mean flow to the oscillating flow near the contact line.

I. INTRODUCTION

It is common knowledge that prescribing an orbital motion to a glass of wine generates a rotating gravity wave that comes along with a swirling mean flow [1]. This mean flow rotates in the direction of the wave and recirculates poloidally (radially and vertically), thus permanently pushing new fluid to the surface where it aerates and releases the wine's aromas [2, 3]. Precisely the same kind of orbital shaking is used on a more professional level in bioreactors for the cultivation of biological cells [4]. There, the presence of the mean flow prevents sedimentation and ensures efficient gas exchange, avoiding the damagingly high shear rates that immersed stirrers would cause.

Because of its importance in engineering applications, experimental and numerical efforts have been made to optimize the mixing efficiency and power consumption of orbital shakers [5–7]. Most of the studies focus on the strongly nonlinear regime (forcing frequency close to the fundamental resonance frequency of the container), and in complex container geometries such as Erlenmeyer flasks with baffles. Near resonance, the rotating wave becomes large and displays complex nonlinear phenomena such as wave breaking and hysteresis [3]. Note that a rotating wave can also be triggered near resonance in a linearly shaken container through a symmetry breaking mechanism [8–10]. Recent experimental advances using particle image velocimetry (PIV) measurements in the frame of the container now allow for quantitative mixing diagnostics in this system (turbulent intensity, local energy dissipation rate) [11, 12].

Recently, numerical and experimental efforts have been devoted to understand the orbital sloshing flow in a simple cylindrical container on a more fundamental level [3, 13]. Whenever the forcing frequency is far enough from a natural frequency of a free gravity wave, the forced rotating wave is well described by inviscid linear potential theory, and corresponds to a superposition of two linear sloshing modes in quadrature [1, 3, 14, 15]. In spite of these experimental and numerical efforts, no general picture is available yet for the mechanism that generates the mean mass transport induced by orbital shaking and its dependence with the flow parameters (aspect ratio of the container, fluid viscosity, forcing amplitude).

Mean mass transport under forced surface waves is a classical problem of fluid mechanics that received much attention mainly because of its oceanographical interest — see for example Refs. [16–19] for historical work on long propagative gravity waves, or Refs. [20, 21] for more recent studies on parametrically excited capillary-gravity waves. Here, we focus on the weakly nonlinear limit, where the amplitude of the waves, harmonics and mean flows can be ranked in decreasing orders of magnitude. In this regime, mean mass transport has two distinct origins: (steady) streaming and Stokes drift. Both contributions add up into what is called the Lagrangian mean flow, and it is difficult in general to anticipate whether transport due to the Stokes drift reinforces or weakens that due to the streaming [22].

In incompressible fluids, streaming is essentially the reaction of the flow to the time-averaged non-linear advection $\overline{\mathbf{u}_w \cdot \nabla \mathbf{u}_w}$, where \mathbf{u}_w denotes the linear wave flow [17, 23]. In the case of potential gravity waves, this basic principle becomes rather subtle, because potential waves do not carry vorticity and as such cannot generate a mean flow in the bulk. Only in the oscillatory (Stokes) boundary layers over the container walls and below the liquid surface a non-zero forcing of a streaming flow can take place, and theoretical modeling there becomes highly non-trivial in three-dimensional contexts [24]. An estimate for the steady streaming magnitude can be obtained as follows. The oscillating boundary layers have a typical thickness $\delta = (\nu/\Omega)^{1/2}$, with Ω the wave frequency and ν the kinematic viscosity. When the amplitude (or phase) of the wave varies along that boundary, mass conservation requires that there must exist a small oscillating flow normal to the boundary. This flow, called boundary layer pumping, is of order $u_w \delta/L$, where L is the lengthscale over which u_w varies. Since the tangential and normal velocities in the boundary layer are not out of phase in general, their average product is non-zero and induce an effective Reynolds stress of order $u_w^2 \delta/L$ that forces a non-zero mean flow in the bulk. The structure of this streaming flow depends on the details of the boundary conditions, but its magnitude \bar{u} can be inferred, at least in the weak steady streaming limit (i.e., for small streaming Reynolds number $\bar{u}L/\nu \ll 1$), from a balance between the Reynolds stress and the viscous stress $\nu \bar{u}/\delta$

at the boundaries, yielding

$$\bar{u} \sim \frac{u_w^2}{\Omega L}. \quad (1)$$

Interestingly, the amplitude of this streaming flow is independent of viscosity, although viscosity is a necessary ingredient for the formation of the Stokes layers from which it originates. We recall that this estimate only applies in the weak streaming limit ($\bar{u}L/\nu \ll 1$), for which the wave properties remain unaffected by the weak mean flow. On the other hand, in the strong streaming regime, the streaming flow can alter the waves, and inertial effects must be considered to solve for the mean flow dynamics [19].

In addition to this (Eulerian) streaming flow contribution, mean mass transport also includes a purely kinematic (Lagrangian) contribution, the Stokes drift [25]. Fluid particles in oscillatory flows move along gyring trajectories and experience, along these paths, slight variations in the wave magnitude. This causes them to displace slightly more in one direction and leads to a small mean drift after each wave period. A noticeable property of the Stokes drift is that it allows mean mass transport even for a zero mean Eulerian flow. An estimate for the Stokes drift velocity can be simply obtained by multiplying the gyration radius of the particles u_w/Ω with the spatial gradient of the wave amplitude u_w/L : it turns out to coincide with Eq. (1), indicating that the Stokes drift and the steady streaming are expected to be of the same order in the case of potential waves.

Although predicting the structure of the mean flow is a difficult task in the orbital sloshing configuration, the above scaling argument (1) can be readily applied to predict its amplitude, at least in the weakly nonlinear regime. Since in this regime the mean flow does not depend on viscosity, a rough estimate can be obtained by using potential flow theory. In a cylinder of radius R , orbitally shaken along a path with circular radius A , and for forcing frequency Ω small compared to the natural frequency ω_1 of the first sloshing mode of the cylinder, the non-dimensional wave amplitude is estimated as [3, 14, 15],

$$\frac{u_w}{\Omega R} \sim \frac{\epsilon}{(\omega_1/\Omega)^2 - 1}, \quad (2)$$

where $\epsilon = A/R \ll 1$ is the non-dimensional forcing amplitude. According to Eq. (1), this wave is therefore expected to generate a Lagrangian mean flow of order

$$\frac{\bar{u}}{\Omega R} \sim \frac{\epsilon^2}{[(\omega_1/\Omega)^2 - 1]^2}. \quad (3)$$

This indicates that the mean flow increases very rapidly with Ω , at least as $\bar{u} \sim \Omega^5$ far from the resonance, and that it does not depend on viscosity. This scaling is compatible with the calculation of Hutton [1] for the Stokes drift associated to the potential flow solution. However, this simplified potential Stokes drift solution corresponds to a purely azimuthal mean flow, lacking the poloidal recirculation, so it cannot provide a complete description of the complex mean flow patterns found in the experiments.

In this paper, we present a systematic series of experiments to determine the structure and the scaling of the wave flow and the mean flow in the weakly nonlinear regime. The mean flow is determined using stroboscopic PIV, i.e. PIV synchronized with the forcing, which naturally filters out the wave motion. We carefully discuss some key aspects of stroboscopic PIV: being a Lagrangian method, it cannot discriminate the Stokes drift from the streaming flow; moreover, the measured mean flow is affected by a systematic bias due to the arbitrary phase of the acquisition, which can be removed here using the axisymmetry of the mean flow. By varying the forcing amplitude ϵ and frequency Ω/ω_1 , we show that the amplitude of the global rotation near the center is well described by Eq. (3) with weak influence of viscosity, and that its structure is compatible with a dominant Stokes drift contribution. On the other hand, we find that the spatial structure of the poloidal vortices near the contact line show strong variations with viscosity and forcing frequency, suggesting a subtle response to the oscillating flow near the contact line.

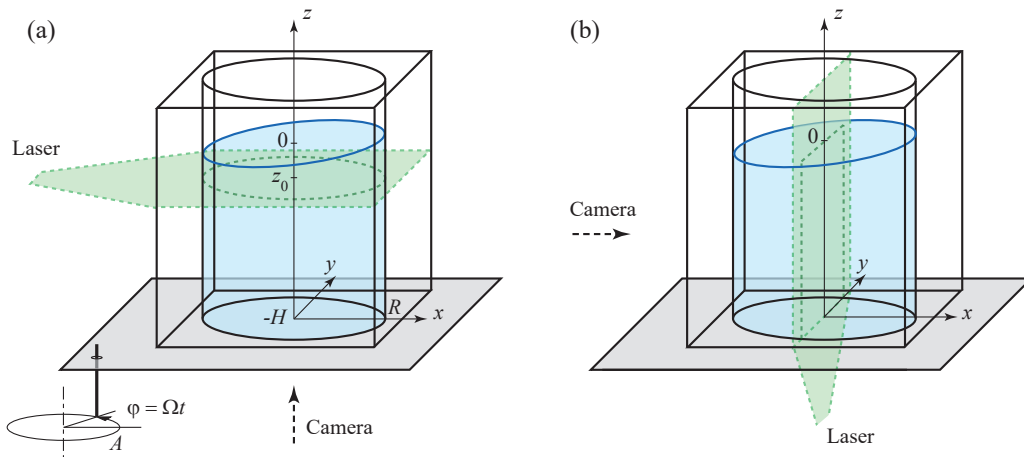


FIG. 1. Experimental setup. The cylinder of radius $R = 51.2$ mm is filled up to a height $H = 111$ mm by silicon oil of kinematic viscosity ν . The entire system is oscillated at a constant frequency Ω along a circular trajectory of radius A , maintaining a fixed orientation with respect to an inertial frame of reference. The particle image velocimetry measurements are performed using a laser sheet (dashed green) and a camera fixed in the laboratory frame. (a) Horizontal measurements in the plane $z_0/R = -0.23$, for the wave flow and the mean flow; (b) Vertical measurements, for the mean flow only.

II. EXPERIMENTAL SET-UP & PROCEDURE

The experimental set-up is sketched in Fig. 1. A glass cylinder of inner radius $R = 51.2$ mm is filled at height $H = 111$ mm with silicon oil of kinematic viscosity $\nu = 50$ or 500 $\text{mm}^2 \text{s}^{-1}$ and surface tension $\gamma = 21 \times 10^{-3}$ N m^{-1} . The cylinder is located on a transparent plate attached to an eccentric motor that shakes the entire system at angular frequency Ω and along a circle of radius A . We choose the origin of time such that an arbitrary point of the container follows the path $\mathbf{r}_c(t) = \mathbf{r}_c(0) + A(\cos \Omega t \mathbf{e}_x + \sin \Omega t \mathbf{e}_y)$. In the co-moving frame attached to the cylinder, this induces an effective gravitational acceleration $\mathbf{g}'(t) = -g\mathbf{e}_z + A\Omega^2(\cos \Omega t \mathbf{e}_x + \sin \Omega t \mathbf{e}_y)$. The shaking amplitude A is varied between 0.3 and 10 mm with precision 0.1 mm and the shaking frequency Ω can be set between 0 and 270 rpm with precision 0.1 rpm. However, measurements for $\Omega < 90$ rpm were found to be hindered by weak fluid motions, of the order of 0.2 mm s^{-1} , due to residual thermal convection in the cylinder, so measurements are restricted to $\Omega > 90$ rpm in the following.

The system is characterized by five non-dimensional numbers,

$$h = \frac{H}{R} = 2.17, \quad \epsilon = \frac{A}{R} \in [0.006, 0.20], \quad Bo = \frac{\rho g R^2}{\gamma} = 1100$$

$$Re = \frac{\Omega R^2}{\nu} \in [50, 1500], \quad Fr = \frac{A\Omega^2}{g} \in [0.0027, 0.8]. \quad (4)$$

We recognize the aspect ratio h of the fluid column, the non-dimensional forcing amplitude ϵ , the Bond number Bo (squared ratio of the cylinder radius to the capillary length), the Reynolds number Re and the Froude number Fr . In the following, we can assume that capillary effects are negligible ($Bo \gg 1$) and that the fluid is nearly inviscid ($Re \gg 1$).

To perform PIV measurements, we seed the fluid with silver-coated neutrally buoyant particles, and illuminate it by a pulsed laser sheet, either vertical or horizontal (see Fig. 1). To minimize refraction through the curved wall, the cylinder is immersed in a cubic container, filled with the same silicon oil. For horizontal measurements (Fig. 1a), the flow is imaged from below, and the laser sheet is located at a height $z_0 = -12$ mm below the surface at rest. This slightly decreases the flow magnitude but is necessary to avoid intersection of the laser sheet with the wavy free surface. Images are mirrored in the following to appear in the right coordinate system (x, y) . For vertical measurements (Fig. 1b), the laser sheet is emitted from below, and the flow is imaged from the side, in the plane (y, z) , at times

$\Omega t_n = \pi/2 + 2n\pi$ for which the cylinder axis crosses the laser sheet.

Velocity fields are computed from PIV using two different schemes for the wave flow and for the mean flow:

(i) The wave flow is measured using conventional PIV, i.e. with a time delay between images that is small compared to the forcing period. This method is essentially insensitive to the mean flow, and provides to a good approximation the Eulerian wave flow.

(ii) The mean flow is measured using stroboscopic PIV, i.e. with image acquisition synchronized with the forcing, in order to filter out the wave motion. This method, similar to that used recently by Perinet *et al.* [20] in Faraday wave experiments, essentially measures the total Lagrangian mean flow (see Sec. IV).

Since the PIV setup (laser and camera) is in the laboratory frame, measurements of the vertical structure of the wave flow cannot be performed, so only measurements in a horizontal plane are achieved. On the other hand, for the mean flow, measurements can be performed both in the horizontal plane (mean rotation) and in the vertical plane (mean poloidal recirculation), because the synchronization of image acquisition with the cylinder motion naturally cancels the contribution due to the cylinder velocity.

Care was taken to ensure the damping of transients before PIV acquisition. Preliminary experiments have shown that the convergence of the wave flow to a stationary regime is achieved very rapidly, after less than 10 forcing periods for $\nu = 50 \text{ mm}^2 \text{ s}^{-1}$. On the other hand, the convergence of the mean flow is achieved on a much slower time scale, after typically 1000 forcing periods (10 minutes). In the following, we wait at least 10 minutes between each measurement.

III. ROTATING WAVE FLOW

A. Inviscid potential solution

We briefly recall here the main results of the potential theory, obtained by summing two linear sloshing solutions with $\pi/2$ phase shift [3, 14]. With the mentioned convention on time, the velocity potential in the reference frame of the cylinder writes

$$\frac{\phi(r, \theta, z, t)}{\Omega R^2} = 2\epsilon \sin(\theta - \Omega t) \sum_{n=1}^{\infty} \alpha_n J_1(k_n r/R) \cosh[k_n(z + H)/R], \quad (5)$$

with

$$\alpha_n = \frac{1}{(k_n^2 - 1)[(\omega_n/\Omega)^2 - 1]J_1(k_n) \cosh(k_n H/R)}. \quad (6)$$

In the spatial structure of this potential, we recognize the potential of free gravity waves, with azimuthal wavenumber $m = 1$ and finer structures in the radial direction as n increases. The numbers k_n are the n th zeros of the derivative of J_1 , the Bessel's function of the first kind and first order ($k_1 \simeq 1.841$, $k_2 \simeq 5.331\dots$). The natural frequencies of these gravity waves are given by

$$\omega_n^2 = \frac{gk_n}{R} \tanh\left(\frac{k_n H}{R}\right). \quad (7)$$

The velocity field in the reference frame of the cylinder, $\mathbf{u} = \nabla\phi$, is

$$\begin{aligned} \frac{u_r}{\Omega R} &= 2\epsilon \sin(\theta - \Omega t) \sum_{n=1}^{\infty} \alpha_n k_n J_1'(k_n r/R) \cosh[k_n(z + H)/R], \\ \frac{u_\theta}{\Omega R} &= 2\epsilon \cos(\theta - \Omega t) \sum_{n=1}^{\infty} \alpha_n k_n \frac{J_1(k_n r/R)}{k_n r/R} \cosh[k_n(z + H)/R], \\ \frac{u_z}{\Omega R} &= 2\epsilon \sin(\theta - \Omega t) \sum_{n=1}^{\infty} \alpha_n k_n J_1(k_n r/R) \sinh[k_n(z + H)/R]. \end{aligned} \quad (8)$$

Obviously, the linear potential theory only holds for Ω far from the natural frequencies ω_n , since otherwise $\alpha_n \rightarrow \infty$ and viscous or nonlinear effects must be considered to regularize the theory. For low forcing frequencies $\Omega \ll \omega_1$, far enough under the first resonance, the wave is dominated by the first mode $n = 1$. We see that in this regime the wave amplitude u_w scales as Eq. (2), as discussed in the Introduction. In the following we will use $(\epsilon, \Omega/\omega_1)$ as control parameters; the normalized frequency Ω/ω_1 is trivially related to Fr , h and ϵ , but is of more practical use. In our set-up, the frequency of the first resonance is $\omega_1 = 180$ rpm and we can cover the interval $\Omega/\omega_1 \in [0.5, 1.5]$.

Viscous effects are absent in this potential model, but we expect that, in the limit of large Re and far enough from resonance, the inviscid linear solution (9) provides a reasonable description of the wave flow far from the boundaries. Near the wall and under the free surface, boundary layers of thickness $\delta = \sqrt{\nu/\Omega}$ develop in order to meet no-slip and free-surface boundary conditions. We expect that viscous damping therein reduces the wave amplitude and introduces a phase shift with respect to the forcing, as observed in linear sloshing problem [26].

B. Experimental measurements

To measure the wave component of the flow, pairs of images separated by a small time lag are taken at each forcing period n in the horizontal plane, such that the average acquisition times for each pair are $\Omega t_n = \pi/2 + 2\pi n$. The velocity fields are averaged over 100 periods. Since the measurements are performed in the laboratory frame, the measured velocity field includes the velocity of the cylinder, $\mathbf{u}_c(t_n) = d\mathbf{r}_c/dt(t_n) = A\Omega[-\sin(\Omega t_n)\mathbf{e}_x + \cos(\Omega t_n)\mathbf{e}_y] = -A\Omega\mathbf{e}_x$ (see Fig. 2a). We simply deduce the wave velocity field in the cylinder frame by subtracting \mathbf{u}_c from the measured velocity fields.

Figure 2(c,d) shows the wave fields for the two fluid viscosities $\nu = 50$ and $500 \text{ mm}^2 \text{ s}^{-1}$, obtained for a forcing frequency $\Omega/\omega_1 = 0.67$ and amplitude $A = 2.9 \text{ mm}$ ($\epsilon = 0.057$). The corresponding Reynolds numbers are $Re = 660$ and 66 , respectively. These wave fields are in good qualitative agreement with the potential solution, shown in Fig. 2(b), except for two features: first, boundary layers are clearly visible at the cylinder wall, of typical thickness 4 and 12 mm respectively, which corresponds to $\simeq 2.5\sqrt{\nu/\Omega}$. Second, we observe a significant phase delay between the wave velocity and the cylinder velocity (which is along $-\mathbf{e}_x$ at this phase), of order $\Delta \simeq 30^\circ$ for the larger viscosity case. Such phase delay was also reported by Ducci *et al.* [12], for different fluid viscosity and aspect ratio.

The amplitude and the phase delay of the wave field have been systematically measured for a forcing frequency Ω/ω_1 in the range $0.5 - 1.5$, at a fixed forcing amplitude $\epsilon = 0.057$. Figure 3(a) compares the wave amplitude, defined as the norm of the horizontal velocity at the center, $|\mathbf{u}_\perp|(r=0) = \sqrt{u_r^2 + u_\theta^2}$, to the potential theory,

$$\frac{|\mathbf{u}_\perp|(r=0, z=z_0)}{\Omega R} = \epsilon \sum_{n=1}^{\infty} \alpha_n k_n \cosh[k_n(z_0 + H)/R], \quad (9)$$

obtained by taking $J_1(x) \simeq x/2$ for $x \rightarrow 0$ in Eq. (9). A good agreement is found at moderate forcing frequency, in the narrow range $\Omega/\omega_1 \in [0.6, 0.8]$. For lower frequency, the determination of the wave velocity is limited by the subtraction of the cylinder velocity $|\mathbf{u}_c|/\Omega R = \epsilon$, which becomes larger than the wave velocity. At larger frequency, the measured wave amplitude is smaller than the potential prediction, which diverges at $\Omega/\omega_1 = 1$. For the larger viscosity, the divergence is clearly smoothed, with a maximum wave amplitude shifted at $\Omega/\omega_1 \simeq 1.1$. For the smaller viscosity, there is a range of frequency around the resonance, $\Omega/\omega_1 \in [1.05, 1.25]$, in which the wave amplitude is too strong and cannot be measured by PIV (the free surface intersects the laser sheet). Outside this range we observe an asymmetric resonance curve, which can be attributed to an hysteresis of the wave above the resonance (only measurements for increasing forcing frequency are shown), in good agreement with the results of Reclari *et al.* [3].

The phase delay Δ between the forcing and the wave velocity, defined as the angle between the fluid velocity at the center of the cylinder and $-\mathbf{e}_x$, is plotted in Fig. 3(b) as a function of the forcing frequency. According to the potential theory, the wave is in phase with the

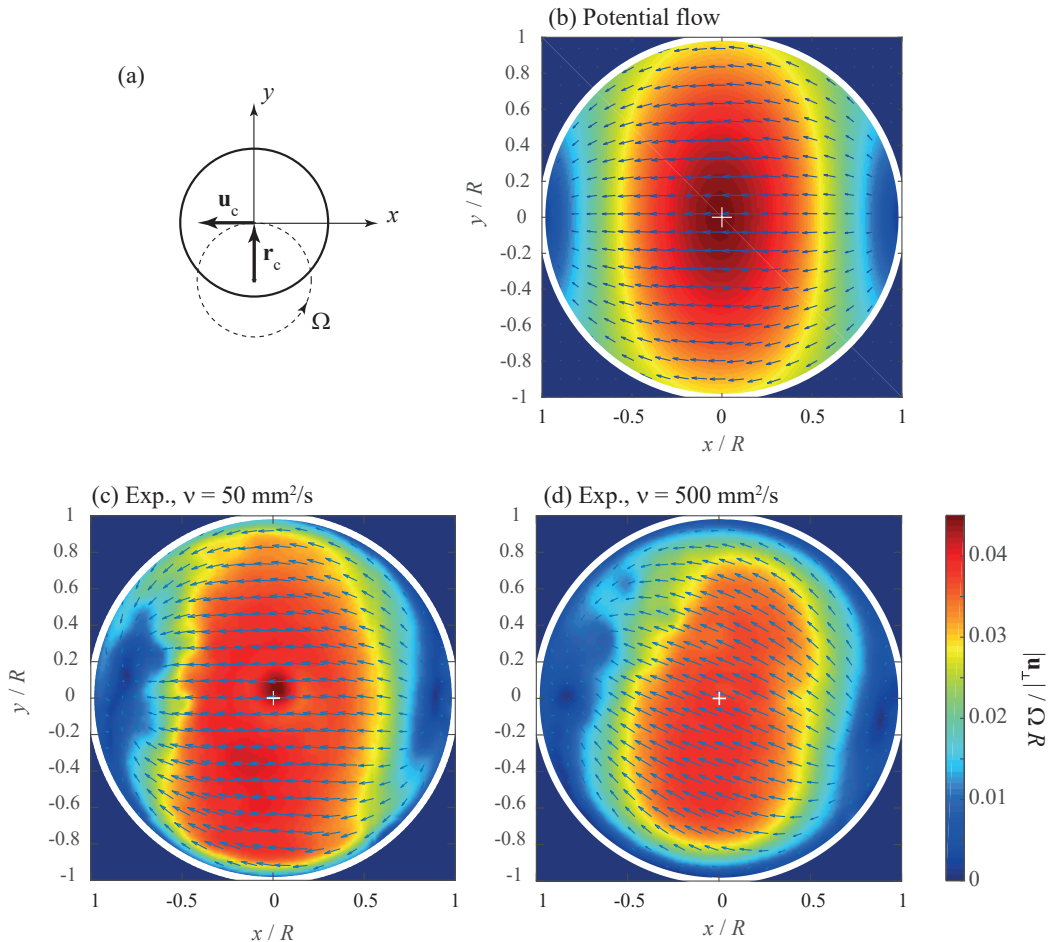


FIG. 2. (a) Orbital motion of the cylinder; the velocity fields in (b)-(d) are taken at phase $\varphi_0 = \pi/2$, for which the cylinder velocity \mathbf{u}_c is along $-\mathbf{e}_x$. (b) Potential flow solution. (c,d) Experimental wave field in the frame of the cylinder, measured at a distance $z_0/R = -0.23$ below the surface, for forcing frequency $\Omega/\omega_1 = 0.67$, forcing amplitude $\epsilon = A/R = 0.057$, and fluid viscosity (c) $\nu = 50$, (d) $\nu = 500 \text{ mm}^2 \text{ s}^{-1}$. The colormap represents the horizontal norm of the velocity.

forcing for $\Omega < \omega_1$ ($\Delta = 0$), whereas it is out of phase for $\Omega > \omega_1$ ($\Delta = 180^\circ$). Here again, we observe that viscosity smoothes the jump of the phase delay around the resonance.

Finally, the linear scaling with respect to the forcing amplitude ϵ in Eq. (2) is checked by varying ϵ in the range $0.006 - 0.20$ at fixed forcing frequency Ω . Results are plotted in Fig. 3(c) for the most viscous fluid. We find a good agreement between experiments and the potential prediction (9) at moderate frequency, $\Omega/\omega_1 = 0.67$ and 0.78 , over the whole range of ϵ . At larger frequency, however, the wave amplitude is below the potential theory, and the linear increase with ϵ starts to saturate for the largest values of ϵ .

IV. MEAN MASS TRANSPORT

A. Interpreting stroboscopic PIV measurements

We now turn to the mean flow generated by the orbital sloshing wave, in the range of parameters $(\epsilon, \Omega/\omega_1)$ for which the potential theory provides a reasonable description of the wave flow. The mean flow contains both the Eulerian contribution (steady-streaming) and the Lagrangian contribution (Stokes drift), that cannot be discriminated by stroboscopic PIV measurements. It is instructive to see why.

Let $\mathbf{u} + \bar{\mathbf{u}}_{str}$ be the total Eulerian velocity field, composed of the time-periodic wave flow

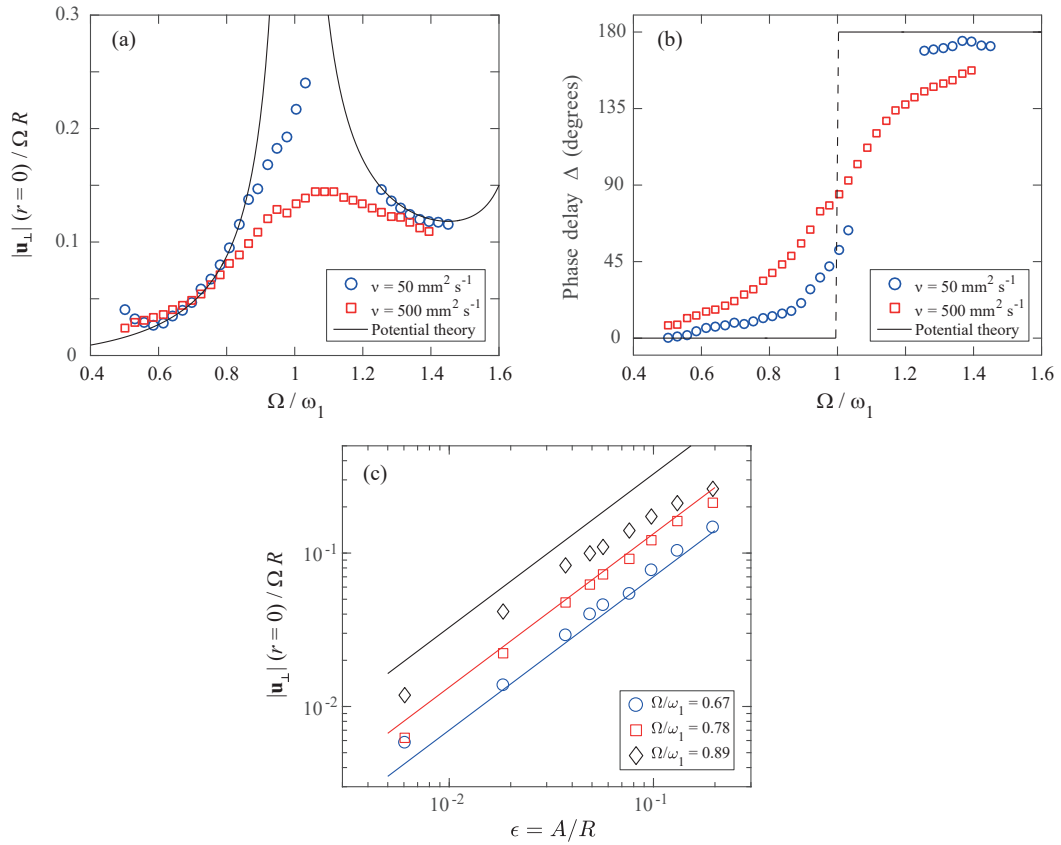


FIG. 3. (a) Norm of the wave velocity measured at $r = 0$, $z_0/R = -0.23$, as a function of the forcing frequency Ω/ω_1 at a fixed forcing amplitude $\epsilon = 0.057$, for the two fluid viscosities. (b) Phase delay Δ between the forcing and the wave field at $r = 0$. (c) Norm of the wave velocity as a function of the forcing amplitude ϵ at three values of the forcing frequency, for $\nu = 500 \text{ mm}^2 \text{ s}^{-1}$. Solid lines show the potential theory prediction (9).

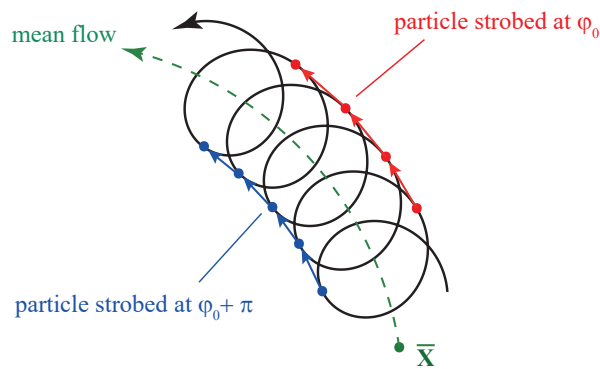


FIG. 4. In the weakly nonlinear regime, the particle trajectory (thick black line) is the sum of a strong oscillating flow \mathbf{u}_w , of order ϵ , and a weak mean flow $\bar{\mathbf{u}}$ (dashed green line), of order ϵ^2 ; the mean flow contribution is exaggerated here for clarity. When imaged at a given phase of the wave (here φ_0 in red and $\varphi_0 + \pi$ in blue), stroboscopic PIV introduces a systematic bias in the determination of the mean flow, of order ϵ^3 . The true mean trajectory $\bar{\mathbf{X}}(t)$ can be reconstructed by averaging the particle displacements over the two phases.

$\mathbf{u}(\mathbf{x}, t)$ of order ϵ and the steady streaming flow $\bar{\mathbf{u}}_{str}(\mathbf{x})$ of order ϵ^2 . We consider a particle that follows the path $\mathbf{X}(t)$ and is imaged at positions $\mathbf{X}(t_n), \mathbf{X}(t_{n+1})$ at times t_n, t_{n+1} separated by precisely one period $T = 2\pi/\Omega$ (see Fig. 4). The mean velocity of the particle measured by stroboscopic PIV then corresponds to

$$\mathbf{u}_{SPIV} = \frac{\mathbf{X}(t_{n+1}) - \mathbf{X}(t_n)}{T} = \frac{1}{T} \int_{t_n}^{t_{n+1}} [\mathbf{u}(\mathbf{X}(t), t) + \bar{\mathbf{u}}_{str}(\mathbf{X}(t))] dt. \quad (10)$$

We introduce a first order estimate of the trajectory

$$\mathbf{X}(t) \approx \bar{\mathbf{X}} + \boldsymbol{\eta}(\bar{\mathbf{X}}, t) + O(\epsilon^2) \quad , \quad \boldsymbol{\eta}(\bar{\mathbf{X}}, t) = \int_{t_n}^t \mathbf{u}(\bar{\mathbf{X}}, t') dt'. \quad (11)$$

Here $\bar{\mathbf{X}}$ is the average particle position over that period and the field $\boldsymbol{\eta}$ is the particle excursion of order ϵ , around this mean position. We use this estimate of $\mathbf{X}(t)$ to reexpress the integrand of (10) using a Taylor expansion around the mean position $\bar{\mathbf{X}}$. Using the periodicity of $\mathbf{u}(\bar{\mathbf{X}}, t)$ and $\boldsymbol{\eta}(\bar{\mathbf{X}}, t)$ we find that

$$\mathbf{u}_{SPIV} = \bar{\mathbf{u}}_{str}(\bar{\mathbf{X}}) + \underbrace{\frac{1}{T} \int_{t_n}^{t_{n+1}} \boldsymbol{\eta} \cdot \nabla \mathbf{u}|_{\bar{\mathbf{X}}} dt}_{\bar{\mathbf{u}}_{Sto}(\bar{\mathbf{X}})} + O(\epsilon^3). \quad (12)$$

The leading order contribution is therefore the sum of the streaming velocity $\bar{\mathbf{u}}_{str}$ and the Stokes drift contribution $\bar{\mathbf{u}}_{Sto}$, which cannot be separated in stroboscopic PIV measurements.

Computing the steady streaming flow $\bar{\mathbf{u}}_{str}$ in the orbital sloshing configuration is a difficult task and requires a dedicated analysis. On the other hand, the Stokes drift $\bar{\mathbf{u}}_{Sto}$ far from the boundaries can be computed to a good approximation from the inviscid wave solution [1]. Denoting $\mathbf{u} = \mathbf{v} \exp(i\Omega t) + c.c.$, we have $\boldsymbol{\eta} = \mathbf{v} \exp(i\Omega t)/(i\Omega) + c.c.$, and the Stokes drift can be simply expressed as

$$\bar{\mathbf{u}}_{Sto} = \frac{2}{\Omega} \text{Im}(\mathbf{v} \cdot \nabla \mathbf{v}^*), \quad (13)$$

where Im stands for imaginary part and the stars indicate complex conjugate. Using this formula, it is easy to see that only the azimuthal component of the drift,

$$\bar{u}_{sto,\theta} = \frac{2}{\Omega} \text{Im} \left(v_r \frac{\partial v_\theta^*}{\partial r} + \frac{v_\theta}{r} \frac{\partial v_\theta^*}{\partial \theta} + v_z \frac{\partial v_\theta^*}{\partial z} + \frac{v_\theta v_r^*}{r} \right)$$

is non-zero and equal to

$$\bar{u}_{sto,\theta} = \epsilon^2 \left\{ \left[\sum_{n=1}^{+\infty} \alpha_n \frac{k_n^2}{2} [J_1(\dots) + J_3(\dots)] \cosh(\dots) \right] \left[\sum_{n=1}^{+\infty} \alpha_n k_n J_2(\dots) \cosh(\dots) \right] + \left[\sum_{n=1}^{+\infty} \alpha_n k_n^2 [J_0(\dots) + J_2(\dots)] \sinh(\dots) \right] \left[\sum_{n=1}^{+\infty} \alpha_n k_n J_1(\dots) \sinh(\dots) \right] \right\}, \quad (14)$$

where the omitted arguments of the Bessel and hyperbolic functions are $k_n r/R$ and $k_n(z+H)/R$, respectively. This indicates that poloidal recirculations found in the experiment can only be due to the steady streaming flow or to viscous corrections of the Stokes drift.

B. Phase bias in stroboscopic PIV measurements

Figure 5(a,b) shows the mean flow at phase $\varphi_0 = \pi/2$, measured in the horizontal plane, at a distance $z_0/R = -0.23$ below the free surface, and in the vertical plane. The mean flow is mainly azimuthal, but with a slightly off-centered minimum velocity. The recirculation in the vertical plane, mostly active in the upper half of the cylinder, is composed of a

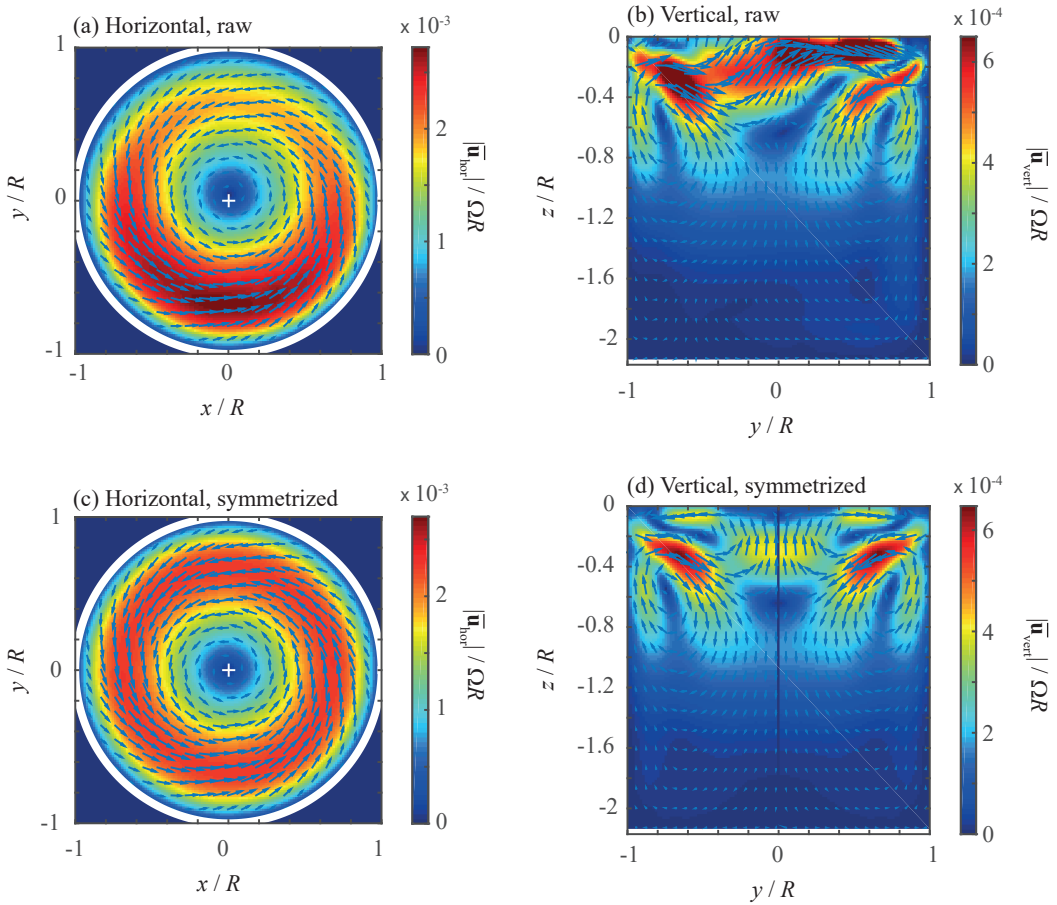


FIG. 5. Mean flow measured by stroboscopic PIV, (a,c) in the horizontal plane at $z_0/R = -0.23$ below the free surface, and (b,d) in the vertical plane. Forcing frequency $\Omega/\omega_1 = 0.67$, amplitude $\epsilon = 0.057$, viscosity $\nu = 500 \text{ mm}^2 \text{ s}^{-1}$. The upper line (a,b) shows the raw velocity fields, and the lower line (c,d) shows the symmetrized velocity fields using Eq. (16) to account for the wave contribution.

nearly axisymmetric toroidal vortex, ascending near the cylinder wall and descending along the axis, together with a strong non-axisymmetric surface current. For these parameters ($\Omega/\omega_1 = 0.67$, $\epsilon = 0.057$), the azimuthal velocity is $\simeq 2 \times 10^{-3} \Omega R$, and the radial and vertical velocities are $\simeq 6 \times 10^{-4} \Omega R$: as expected this mean flow is much smaller than the wave flow, which is of order of $5 \times 10^{-2} \Omega R$ here (see Fig. 3).

The axisymmetry breaking in the mean flow originates from a bias in the stroboscopic PIV method, which we illustrate in Fig. 4: the particle displacement during one oscillation period contains, for a non-homogeneous wave flow, a contribution which depends on the arbitrary acquisition phase φ_0 . This highlights a real subtlety in stroboscopic PIV: although the previous manipulations (12) show that \mathbf{u}_{SPIV} provides a measure of the Lagrangian mean flow, we do not precisely know where that mean flow vector should attach, in $\bar{\mathbf{X}}$, \mathbf{X}_n , \mathbf{X}_{n+1} or somewhere in between. Although the mean particle position $\bar{\mathbf{X}}$ is the most defensible choice, image correlation naturally locates the vector \mathbf{u}_{SPIV} at the phase-dependent particle positions, say at \mathbf{X}_n . Constructing the PIV field from these pointwise measurements therefore introduces a systematic bias, which can be expressed mathematically through the following Taylor expansion

$$\begin{aligned} \mathbf{u}_{\text{SPIV}}(\mathbf{X}_n) &= \mathbf{u}_{\text{SPIV}}(\bar{\mathbf{X}} + \boldsymbol{\eta}(\bar{\mathbf{X}}, t_n) + O(\epsilon^2)) \\ &= \mathbf{u}_{\text{SPIV}}(\bar{\mathbf{X}}) + \boldsymbol{\eta}(\bar{\mathbf{X}}, t_n) \cdot \nabla \mathbf{u}_{\text{SPIV}}|_{\bar{\mathbf{X}}} + O(\epsilon^2). \end{aligned} \quad (15)$$

Attaching the mean flow vector to the instantaneous position \mathbf{X}_n rather than to the mean position $\bar{\mathbf{X}}$ pollutes the mean flow measurement with a systematic bias $\boldsymbol{\eta} \cdot \nabla \mathbf{u}_{\text{SPIV}}$ that

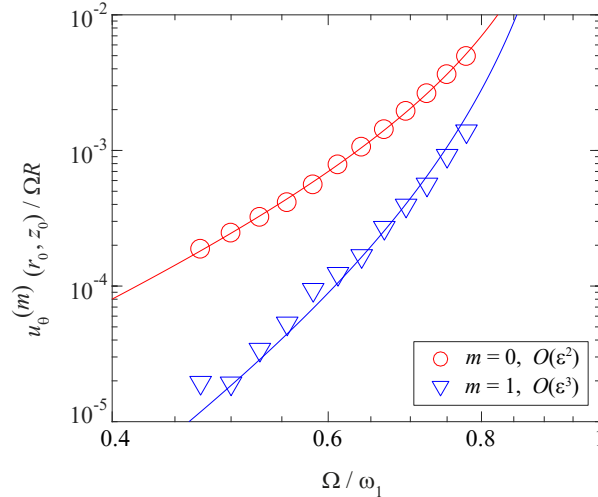


FIG. 6. Amplitude of the modes $m = 0$ (\circ) and $m = 1$ (\triangle) of the azimuthal mean flow at radius $r_0 = R/2$ and height $z_0 = -0.23R$, as measured by stroboscopic PIV, as a function of the forcing frequency Ω/ω_1 at a fixed forcing amplitude $\epsilon = 0.057$, for viscosity $\nu = 500 \text{ mm}^2 \text{ s}^{-1}$. The lines show the best fits with the laws $\epsilon^2/[(\omega_1/\Omega)^2 - 1]^2$ and $\epsilon^3/[(\omega_1/\Omega)^2 - 1]^3$, respectively.

relates to the particle displacement $\boldsymbol{\eta}(\bar{\mathbf{X}}, t_n)$ and to the spatial gradient of the mean flow field in that direction. With \mathbf{u}_{SPIV} of order ϵ^2 , the bias $\boldsymbol{\eta} \cdot \nabla \mathbf{u}_{\text{SPIV}}$ is of order ϵ^3 . In principle, it is possible to measure the field $\mathbf{u}_{\text{SPIV}}(\bar{\mathbf{X}})$ by averaging stroboscopic measurements at many different phases. This costly procedure is however technically impossible in our experiment because the PIV setup is in the laboratory frame and only the two phases when the cylinder axis crosses the laser sheet can be measured.

Even though we cannot filter the bias a whole, we can still filter out the largest contribution to it. We can assume that the bias $\boldsymbol{\eta} \cdot \nabla \mathbf{u}_{\text{SPIV}}$ has a dominant azimuthal wavenumber $m = 1$ and the structure of a travelling wave. Given one biased SPIV field $\mathbf{u}_{\text{SPIV}}(r, \theta, z)$ obtained at any arbitrary phase we can then calculate

$$\bar{\mathbf{u}}(r, \theta, z) = \frac{1}{2} (\mathbf{u}_{\text{SPIV}}(r, \theta, z) + \mathbf{u}_{\text{SPIV}}(r, \theta + \pi, z)). \quad (16)$$

In the horizontal plane, we simply rotate the measured field over π , and in the vertical plane we apply a mirror symmetry with respect to the axis $r = 0$. This procedure cancels all odd m - contributions to the flow field, but leaves all even m contributions invariant, reducing the bias to order ϵ^4 . The validity of this procedure is illustrated in Fig. 6. We have decomposed the azimuthal component of the raw SPIV field, measured along the radius $r_0 = R/2$ at height $z_0 = -0.23R$, as

$$u_{\text{SPIV},\theta}(\theta; r_0, z_0) = u_{\theta}^{(0)} + u_{\theta}^{(1)} \cos(\theta - \theta_0)$$

(with θ_0 an arbitrary phase). The two modal contributions, $u_{\theta}^{(0)}$ and $u_{\theta}^{(1)}$, plotted as a function of the forcing frequency Ω/ω_1 at fixed forcing amplitude ϵ , indeed show the expected scaling, $\epsilon^2/[(\omega_1/\Omega)^2 - 1]^2$ and $\epsilon^3/[(\omega_1/\Omega)^2 - 1]^3$.

The reconstructed mean flow fields, symmetrized using Eq. (16), are shown in Fig. 5(c,d). The poloidal recirculation flow in the vertical plane now appears as two vortices, an upper one with ascending flow near the surface (previously hidden by the wave contribution), and a lower one with descending flow, separated by a stagnation point at $z/R \simeq -0.65$. Note the intense oblique jets that sprout from the contact line region. This picture shows that the radial component in the horizontal plane strongly depends on the height of the measurement plane. For the plane chosen here, $z_0/R = -0.23$, we have $u_r \simeq 0$ near the center and $u_r < 0$ at the periphery, but other situations may be encountered for other values of z (in particular $u_r > 0$ at the free surface).

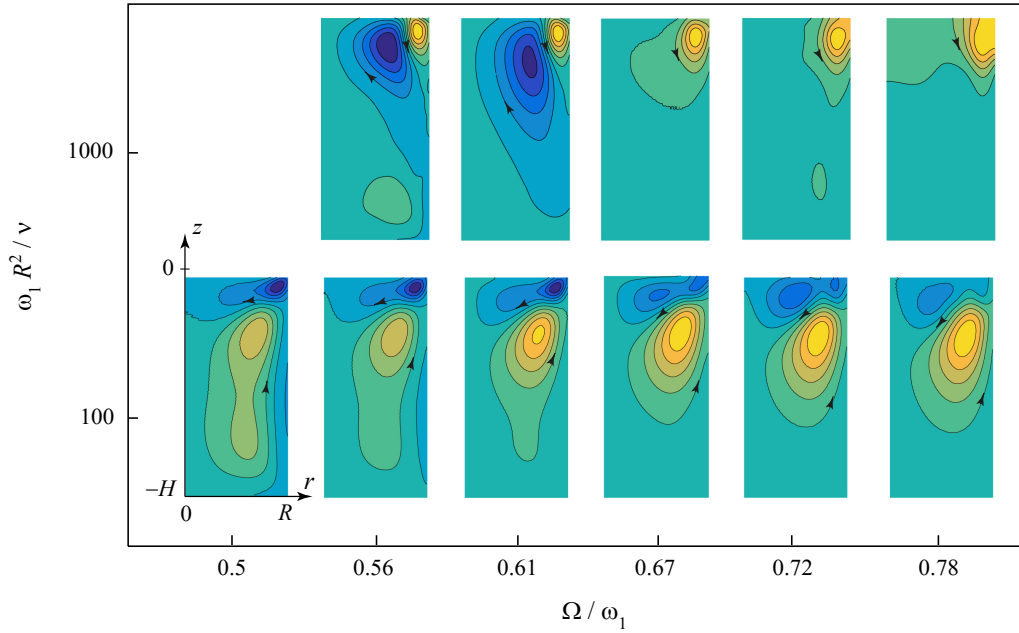


FIG. 7. Streamfunction of the mean flow in the vertical plane, for $\epsilon = 0.057$, for the two fluid viscosities, $\nu = 500$ and $50 \text{ mm}^2 \text{ s}^{-1}$ ($\omega_1 R^2 / \nu = 100$ and 1000 , respectively). In each snapshot the cylinder axis is on the left.

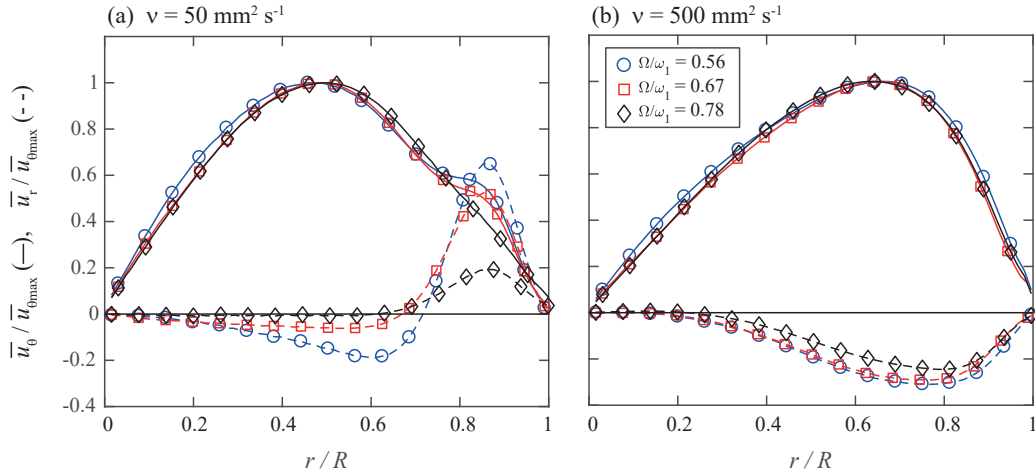


FIG. 8. Radial and azimuthal velocity profiles of the mean flow normalized by the maximum azimuthal velocity, measured at $z_0/R = -0.23$ for $\epsilon = 0.057$, (a) $\nu = 50 \text{ mm}^2 \text{ s}^{-1}$, (b) $\nu = 500 \text{ mm}^2 \text{ s}^{-1}$.

C. Dependence of the mean flow pattern with governing parameters

We have systematically measured the mean flow for the two fluid viscosities, for a forcing amplitude $\epsilon = 0.057$. Here measurements are performed over a restricted range of forcing frequencies, $\Omega/\omega_1 \in [0.5, 0.8]$, for which the wave flow is well described by the linear scaling (2) (see Fig. 3). The mean flow for higher frequencies could not be measured using stroboscopic PIV, because of the particles swept out of the measurement plane after one oscillation period.

The results are summarized in Fig. 7, showing the axisymmetric (Stokes) streamfunction in the vertical plane, and in Fig. 8, showing the radial profiles of the radial and azimuthal

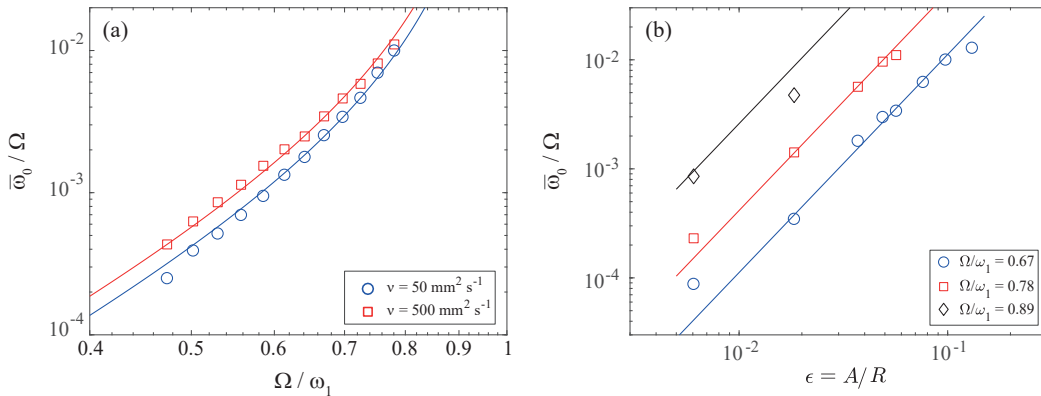


FIG. 9. Mean angular velocity $\bar{\omega}_0$ at $r = 0$, $z_0/R = -0.23$, (a) as a function of the forcing frequency Ω/ω_1 at a fixed forcing amplitude $\epsilon = 0.057$, for the two fluid viscosities; (b) as a function of the forcing amplitude ϵ at three values of the forcing frequency, for $\nu = 500 \text{ mm}^2 \text{ s}^{-1}$. Solid lines show the weakly nonlinear scaling law (17).

components normalized by the maximum azimuthal component at $z_0/R = -0.23$. For both viscosities, the azimuthal velocity profiles are remarkably independent of the forcing frequency. The mean flow is nearly in solid-body rotation near the center, rotating in the direction of the orbital shaking: $\bar{\mathbf{u}} \simeq \bar{\omega}_0 r \mathbf{e}_\theta$ for $r/R < 0.3$, with $\bar{\omega}_0 > 0$ the mean angular velocity. At larger radius, the mean azimuthal velocity decreases and the three velocity components become of the same order, marking the presence of a strong poloidal recirculation vortex near the contact line, where the wave amplitude is larger. A secondary poloidal recirculation vortex of weaker amplitude, located either below or at smaller radius than the primary vortex, is also present. The location and the rotation of these vortices are found to depend both on the viscosity and forcing frequency. As a result, the mean surface velocity near the wall may be either outward (mostly in the viscous case or at moderate forcing frequency) or inward, with the formation of a stagnation circle at the surface in some cases.

Given that the structure of the wave flow does not change much in the studied range of parameters, it is unlikely that the weak streaming limit can explain the observed strong variation of the poloidal mean flow structure. Indeed, the (streaming) Reynolds number based on the mean flow, $Re_s = \bar{u}R/\nu$, is in the range $0.03 - 1$ for $\nu = 500 \text{ mm}^2 \text{ s}^{-1}$, and $0.3 - 10$ for $\nu = 50 \text{ mm}^2 \text{ s}^{-1}$, indicating that the criterion $Re_s \ll 1$ for the weak streaming limit is reasonably satisfied for the more viscous fluid, but not for the less viscous fluid. Accordingly, the complex patterns of poloidal streaming flow in Fig. 7 probably originate from instabilities of the streaming flow, and require to go beyond the weak streaming limit.

This strong dependence of the poloidal flow with the governing parameters makes quantitative comparison with the literature difficult. We can note that the present results are in qualitative agreement with some previous experimental [11] and numerical [13] studies, although obtained for different aspect ratio and ranges of parameters. Weheliye *et al.* [11] observed, in a flat cylinder of aspect ratio $H/R = 0.6$ filled with water forced at $\Omega/\omega_1 = 0.56$ a single poloidal vortex with ascending velocity along the axis, compatible with the observed trend for increasing Reynolds number. In a cylinder of aspect ratio $H/R = 2$ and a weak forcing frequency of $\Omega/\omega_1 = 0.21$, Kim and Kizito [13] observed a similar toroidal vortex with ascending fluid along the axis at small viscosity ($\nu < 3 \text{ mm}^2 \text{ s}^{-1}$), and the formation of an additional counter-rotating poloidal vortex near the wall at larger viscosity ($\nu > 10 \text{ mm}^2 \text{ s}^{-1}$), which again is compatible with our observations.

We now turn to the scaling of the mean flow amplitude as a function of the forcing frequency and amplitude. We characterize the mean flow by its dominant azimuthal contribution near the center: we compute the angular velocity, $\bar{\omega}_0 = \lim_{r \rightarrow 0} \bar{u}_\theta(r)/r$, from the measurements in the horizontal plane at depth $z_0/R = -0.23$. The angular velocity, normalized by the forcing frequency Ω , is plotted as a function of Ω/ω_1 in Fig. 9(a), and as a function of the forcing amplitude ϵ in Fig. 9(b). We first note that the range of variation of

$\bar{\omega}_0$ is considerable: it varies over almost two orders of magnitude in the small range of forcing frequency explored here. Here again, measurement ranges are limited by the sweeping of the particles out of the measurement plane after one period for large values of ϵ and Ω , and by contamination by residual thermal motion for small values of ϵ and Ω . In practice, the largest measurable angular velocity using stroboscopic PIV is $\bar{\omega}_0 \simeq 10^{-2}\Omega$, i.e., the fluid performs one complete rotation after 100 forcing periods.

The amplitude of the mean angular velocity is finally compared with the weakly nonlinear scaling law (3), written in the form

$$\frac{\bar{\omega}_0}{\Omega} = K \frac{\epsilon^2}{[(\omega_1/\Omega)^2 - 1]^2}, \quad (17)$$

with K a tunable non-dimensional constant. In spite of its simplicity, this scaling provides a remarkable description of the data. Viscosity is found to slightly enhance the mean flow, an effect which cannot be accounted for by Eq. (17): best fits with respect to Ω/ω_1 at fixed ϵ , shown in Fig. 9(a), yield $K \simeq 1.1 \pm 0.1$ for $\nu = 50 \text{ mm}^2 \text{ s}^{-1}$ and $K \simeq 1.5 \pm 0.1$ for $\nu = 500 \text{ mm}^2 \text{ s}^{-1}$. The ϵ^2 scaling is also tested in the case $\nu = 500 \text{ mm}^2 \text{ s}^{-1}$, in Fig. 9(b), using the same value of K as in Fig. 9(a). A good overall agreement is obtained at moderate forcing frequency, whereas a mean flow slightly smaller than predicted is obtained as the resonance is approached, which is consistent with the weaker wave amplitude observed in Fig. 3.

It is interesting to compare the fitted values of K with the one we would get with the Stokes drift alone (i.e., with no Eulerian steady streaming). From Eq. (14), and retaining only the first term $n = 1$, we have

$$K_{Sto} \simeq \frac{k_1^4}{2(k_1^2 - 1)^2 J_1^2(k_1)} \frac{\sinh^2(k_1(H + z_0)/R)}{\cosh^2(k_1 H/R)} \simeq 1.25, \quad (18)$$

which is remarkably close to the experimental data, suggesting that the mean zonal circulation is predominantly due to the Stokes drift. This might also explain why the mean azimuthal flow is more robust than the the poloidal recirculation: The Stokes drift being a kinematical effect associated to the waves, it will be essentially not affected by the instabilities of the streaming flow.

V. CONCLUSION

In this paper we characterized the wave flow and the Lagrangian mean flow in an orbitally shaken cylinder in the weakly nonlinear regime. The wave flow, measured by conventional PIV, shows a spatial structure in the bulk and a scaling in amplitude close to the potential prediction for forcing frequency far from the resonance, $\Omega/\omega_1 < 0.8$, except for a significant phase delay which increases with viscosity. The Lagrangian mean flow, measured by stroboscopic PIV, is composed of a robust global rotation near the center, and poloidal recirculation vortices mostly active near the contact line. Far from resonance, the amplitude of the central rotation is well described by a simple weakly nonlinear scaling law, quadratic in forcing amplitude, with a weak dependence on viscosity. This central rotation is mainly due to the Stokes drift, which might explain its robustness, whereas the poloidal recirculations experience a series of bifurcations, with changes in the number of vortices depending on the control parameters of the flow, suggesting unstable streaming flow.

Only scarce comparisons can be performed with literature at the moment, and a full description of the steady streaming flow, even in the weakly nonlinear regime, is not available yet. Such model would require to build the viscous sloshing modes and to compute from them the momentum transfer from the boundary layer region to the bulk. This is a difficult task for three-dimensional flows with free boundaries [20, 24], even in the weak streaming limit, $\bar{u}R/\nu \ll 1$. Considering the complexity and variation of the steady streaming flows observed here, we anticipate that the weak streaming limit likely cannot capture all the observed patterns, and that a nonlinear Craik-Leibovich model [19] seems required. The large amplitude of the mean flow near the contact line is also problematic, since this is a very complex boundary layer region to solve. This specificity has been ignored in [20, 24],

but here our observations suggest that this the contact line region might well be crucial in understanding the spatial structure of the poloidal recirculation. Finally, another difficulty in comparing experiments, numerics and theory may arise from possible surface contamination effects. Although the use of silicon oil in the present experiments is expected to minimize surface contamination, it is known that pure free-slip boundary condition at the surface is extremely difficult to achieve, and that departure from this ideal situation may have dramatic influence in steady streaming [18, 20, 27, 28].

ACKNOWLEDGMENTS

We acknowledge A. Aubertin, L. Auffray, R. Kostenko and R. Pidoux for their experimental help, and D. Cébron, M. Rabaud and A. Sauret for fruitful discussions. F.M. acknowledges the Institut Universitaire de France.

-
- [1] R.E. Hutton, Fluid-particle motion during rotary sloshing, *J. Appl. Mech* **31** (1), 123–130 (1964).
 - [2] M. Reclari, Hydrodynamics of orbital shaken bioreactors, PhD Ecole Polytechnique de Lausanne (2003) http://infoscience.epfl.ch/record/188176/files/EPFL_TH5759.pdf
 - [3] M. Reclari, M. Dreyer, S. Tissot, D. Obreschkow, F.M. Wurm, and M. Farhat, Surface wave dynamics in orbital shaken cylindrical containers, *Phys. Fluids*, **26**, 052104 (2014).
 - [4] D. T. Monteil, G. Tontodonati, S. Ghimire, L. Baldi, D.L. Hacker, C.A. Bürki, F.M. Wurm, Disposable 600-mL orbitally shaken bioreactor for mammalian cell cultivation in suspension, *Biochemical Engineering J.* **76**, 6–12 (2013).
 - [5] J. Büchs, U. Maier, C. Milbradt, B. Zoels, Power consumption in shaking flasks on rotary shaking machines: II. Nondimensional description of specific power consumption and flow regimes in unbaffled flasks at elevated liquid viscosity, *Biotechnology and Bioengineering* **68** (6), 594-601 (2000).
 - [6] C.P. Peter, Y. Suzuki, K. Rachinskiy, S. Lotter, and J. Büchs, Volumetric power consumption in baffled shake flasks, *Chem. Eng. Sci* **61**, 3771-3779 (2006).
 - [7] J. Gardner and G. Tattersson, Characterization of mixing in shaker table containers, *Biotechnology and Bioengineering* **39** (7), 794-797, (1992).
 - [8] F.T. Dodge, The new “Dynamic behavior of liquids in moving containers” (Southwest Research Institute, San Antonio, Texas, 2000). ftp://apollo.ssl.berkeley.edu/pub/ME_Archives/GovernmentandIndustryStandards/NASADocuments/SwRI_Fuel_Slosh_Update.pdf
 - [9] M. Funakoshi and S. Inoue, Surface waves due to resonant horizontal oscillation, *J. Fluid Mech.*, **192**, 219 (1988).
 - [10] A. Royon-Lebeaud, E.J. Hopfinger and A. Cartellier, Liquid sloshing and wave breaking in circular and square-base cylindrical containers, *J. Fluid Mech.*, **577**, 467 (2007).
 - [11] W. Weheliye, M. Yianneskis, and A. Ducci, On the fluid dynamics of shaken bioreactors – flow characterization and transition, *AIChE Journal* **59** (1), 334-344 (2013).
 - [12] A. Ducci, and W.H. Weheliye, Orbitally shaken bioreactors — Viscosity effects on flow characteristics, *AIChE Journal* **60** (11), 3951–3968 (2014).
 - [13] H. Min Kim and J.P. Kizito, Stirring free surface flows due to horizontal circulatory oscillation of a partially filled container, *Chem. Eng. Comm.* **196**, 1300 (2009).
 - [14] R.A. Ibrahim, *Liquid sloshing dynamics: theory and applications* (Cambridge University Press, 2005).
 - [15] O.M. Faltinsen and A.N. Timokha, *Sloshing* (Cambridge University Press, 2014)
 - [16] M.S. Longuet-Higgins, Mass Transport in Water Waves, *Philosophical Transactions of the Royal Society of London. Series A, Mathematical and Physical Sciences* **245** (903), 535 (1953).
 - [17] G.K. Batchelor, *An introduction to fluid dynamics*, (Cambridge University Press, 1967).
 - [18] A.D.D. Craik, The drift velocity of water waves, *J. Fluid Mech.* **116**, 187 (1982).
 - [19] Craik, A. D. and Leibovich, S. A rational model for Langmuir circulations, *J. Fluid Mechanics*, **73**(3), 401-426 (1976).
 - [20] N. Perinet, P. Gutierrez, H. Urra, N. Mujica, L. Gordillo, Streaming patterns in Faraday waves, *subm. to J. Fluid Mech* (2016).
 - [21] M. Higuera, E. Knobloch, J.M. Vega, Dynamics of nearly inviscid Faraday waves in almost circular containers, *Physica D* **201**, 83 (2005).

- [22] E. Larrieu, E.J. Hinch, F. Charru, Lagrangian drift near a wavy boundary in a viscous oscillating flow, *J. Fluid Mech.* **630**, 391 (2009).
- [23] N. Riley Steady Streaming, *Annu. Rev. Fluid Mech.*, **33**, 43 (2001).
- [24] J.A. Nicolás and J.M. Vega, Three-dimensional streaming flows driven by oscillatory boundary layers, *Fluid Dyn. Res* **32** (4), 119 (2003).
- [25] G. G. Stokes, On the theory of oscillatory waves, *Trans. Camb. Phil. Soc.*, **8**, 441-455 (1847).
- [26] Bauer, H. F. and W. Eidel, Free oscillations and response of a viscous liquid in a rigid circular cylindrical tank, *Aerospace science and technology* **3**(8), 495-512 (1999).
- [27] E. Martín and J.M. Vega, The Effect of Surface Contamination on the Drift Instability of Standing Faraday Waves, *J. Fluid Mech.* **546**, 203–225 (2006).
- [28] M. Higuera, J. Porter, F. Varas, and J.M. Vega, Nonlinear Dynamics of Confined Liquid Systems with Interfaces Subject to Forced Vibrations, *Advances in Colloid and Interface Science* **206**, 106 (2014).